2024 IEEE 25th International Workshop on Signal Processing Advances in Wireless Communications (SPAWC) | 979-8-3503-9318-7/24/$31.00 ©2024 IEEE | DOI: 10.1109/SPAWC60668.2024.10694624

Accurate Channel Model for Near Field Terahertz Communications Beyond 6G

(Invited Session Paper)

Vitaly Petrov
Division of Communication Systems
KTH Royal Institute of Technology, Sweden
vitalyp@kth.se

Dmitri Moltchanov
Unit of Electrical Engineering
Tampere University, Finland
dmitri.moltchanov@tuni.fi

Josep Miquel Jornet
Institute for the Wireless Internet of Things
Northeastern University, Boston, MA, USA
j.jornet@northeastern.edu

***Abstract*—Future 6G and beyond-6G cellular systems are expected to operate in the sub-terahertz (0.1–0.3 THz) and terahertz (THz, 0.3–3 THz) frequency bands. However, the small wavelength coupled with large antenna apertures force a part of the (sub-)THz access points coverage to be in the near field. There, conventional far-field propagation models (e.g., free space path loss, FSPL) are not applicable, as their use leads to substantial errors in the analysis. At the same time, existing exact near-field models following the electromagnetic principles are relatively complex and require additional efforts when using them for simple link budget predictions. In this paper, we fill this gap by developing an accurate yet easy-to-use propagation model for near-field THz communications. The proposed model has a simple algebraic structure, is applicable to both near field and far field, and requires no fine-tuning for different sets of input parameters. We analyze the key dependencies in the THz near field channel with the developed model and also contrast the results with those by FSPL, noticing up to 20 dB difference.**

***Index Terms*—THz, Near-field communications, 7G, Path loss.**

I. Introduction

Forthcoming sixth-generation (6G) sub-terahertz (sub-THz, 100 GHz–300 GHz) and beyond-6G terahertz (THz, 300 GHz–3 THz) wireless systems bring not only extraordinary promises but also new challenges [1]. One of them is a non-negligible length of the *near-field zone* in sub-THz and, especially, THz systems [2]. The overwhelming majority of modern wireless communication systems from 1G to 5G operate under the far-field assumption, stating that the phase difference between the component of the transmitted signal coming to one part of the receiver antenna and the component received at the same time by another part of the receiver antenna is negligible [3].

Meanwhile, the prospective (sub-)THz communication systems aiming for decisive coverage will have to maintain or even increase the size of their antenna systems over those used today in 4G and 5G [4]. Such design choice not only makes these (sub-)THz antennas more directional but also immediately increases the length of the near-field zone – the range of distances between the communicating nodes, where the said phase difference is *not negligible anymore* [5].

The exact formula for a widely-used near-field to the far-field boundary, referred to as the Fraunhofer distance, d_{F}, depends on the setup and for the simplest case of a point transmitter and a receiver antenna of maximum dimension D it comes to $d_{\mathrm{F}} = 2D^2/\lambda$, where λ stands for the signal wavelength [3]. Canonical far-field models, including the free space path loss (FSPL) model following the Friis law, cannot be applied in the near field, thus calling for more complex approaches to analyze near-field communication links. Importantly, due to notably shorter λ, envisioned sub-THz and THz communication systems are characterized by the near-field zone of up to several tens of or even hundreds of meters, in contrast to cm-scale or meter-scale near-field zones at lower frequencies [5], [6]. Hence, accounting for the near-field propagation effects in THz communications is important [7].

A conventional approach to characterize the received power in the near-field is the solution of Maxwell's equations [8]. Accordingly, the intensities of the electric and magnetic field are first calculated and then the power is obtained by utilizing Poynting's theorem via integration of the power flow of an electromagnetic field over the arrays' elements [3]. However, the direct theoretical solution of Maxwell's equation is rather complex. In practical applications, the authors resort to numerical approximations such as the finite element method and other grid-based techniques [9] that are implemented in modern software packages. However, such models need to be calculated for a given array's configurations and propagation environments and are characterized by high computational complexity. Thus, they cannot be easily utilized for first-order approximations in performance evaluation and optimization studies for forthcoming (sub-)THz cellular systems.

In this paper, by reformulating the near-field propagation between the transmitter and the receiver antenna arrays as a superposition of multiple far-field communication links between individual array elements, we derive two geometric antenna gain and propagation models for near-field THz communications. These are referred to as Model 1, presenting a direct approach, and Model 2 simplifying the analysis notably without any loss in accuracy. Both models, by design, give exact solutions and, notably, are formulated using the same terms as canonical far-field models. Hence, there is no need for electromagnetic (EM) theory formulas, so the proposed approach is easy to use for communication engineers.

The main contributions of this paper are:

- An exact propagation model is derived for near-field THz communications referred to as Model 2 and characterized by lower complexity than direct calculations (Model 1).
- An illustrative numerical study is performed revealing the key dependencies in the THz near field between the

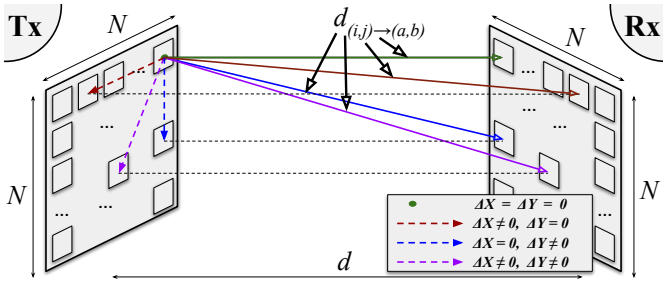

Fig. 1. The considered system model.

system parameters on one side and the antenna gain together with the average received power on the other.

II. System Model

Our system model is illustrated in Fig. 1. It comprises a single (sub-)THz transmitter (Tx) and a single (sub-)THz receiver (Rx) separated by d meters. Both Tx and Rx are equipped with planar antenna arrays of $N \times N$ elements. The arrays are centered and parallel to each other, providing a perfect alignment of non-steered THz beams.

The transmitted signal has the frequency f and the total transmit power P_{Tx}. The spacing between the antenna array elements is $\lambda/2$, where $\lambda = c/f$ is the wavelength and c stands for the speed of light. The physical dimensions of the Tx and Rx 2D arrays are thus $D \times D$ square meters, where $D = N\lambda/2$. For a clear illustration of the near-field effects, we assume operation in one of the THz absorption windows [10], where the impact of the atmospheric absorption is negligible.

For the reference far-field model we utilize the following analytical expression for the received power, $P_{\text{Rx,FF}}$, as a function of the separation distance d, the signal frequency f, and the antenna gains $G_{\text{Tx}} = N^2$ and $G_{\text{Rx}} = N^2$ [3] as:

$$P_{\text{Rx,FF}} = P_{\text{Tx}} G_{\text{Tx}} G_{\text{Rx}} \left(\frac{c}{4\pi f d}\right)^2. \tag{1}$$

For the proposed near-field models, we are interested in both the received signal amplitude as a function of time, $S_{\text{Rx}}(t)$, and the average received power, $P_{\text{Rx}} = \int_{-T/2}^{T/2} E[(S_{\text{Rx}}(t))^2]$, where $T = 1/f$ stands for the signal period.

III. Near Field Propagation Model

A. Geometry of Near-Field Propagation

The canonical model in (1) holds only when the Rx is located in the Tx's far field. However, for distances $d < d_{\text{F}}$, where d_{F} is the Fraunhofer distance [3], the Tx and Rx antennas are in each other's near field, thus compromising the "plane" wave assumption utilized in (1). Thus, (1) cannot be directly applied. The exact value of the near-field boundary by the Fraunhofer distance definition depends on the setup and in our case (two identical 2D arrays with perfect alignment) is equal to $d_{\text{F}} = 16D^2/\lambda$ [7].

To develop the simple and computationally efficient model, we first decompose the Tx antenna array into N^2 individual antennas, each transmitting an attenuated copy of the original signal with power P_{Tx}/N^2, see Fig. 1. We then do the same to the antenna array at the Rx. Now, the setup presents $N^2 \times N^2$ individual propagation paths, where each of the paths is in the far field, as the physical size of the element is small [3].

For tractability, we enumerate Tx antenna array elements in the Tx array as (i, j), where $i \in \{1, 2, \ldots, N\}$ and $j \in \{1, 2, \ldots, N\}$. Similarly, the elements of the Rx array are addressed as (a, b), where $a \in \{1, 2, \ldots, N\}$ and $b \in \{1, 2, \ldots, N\}$. By utilizing the propagation geometry in Fig. 1, we observe that the received power at the Rx's antenna array element (a, b) induced by the emitted power of the Tx's antenna array element (i, j) is given by

$$P_{\text{Rx},(a,b)} = \frac{P_{\text{Tx}}}{N^2} \left(\frac{c}{4\pi f d_{(i,j)\to(a,b)}}\right)^2, \tag{2}$$

where, $d_{(i,j)\to(a,b)}$ is the distance between (i, j)-th element at the Tx and (a, b)-th element at the Rx (see Fig. 1).

As the antenna array spacing is $\lambda/2 = c/2f$, we get

$$d_{(i,j)\to(a,b)} = \sqrt{d^2 + \left(\frac{c}{2f}(a-i)\right)^2 + \left(\frac{c}{2f}(b-j)\right)^2}. \tag{3}$$

Note that these individual N^2 signal components arrive at the Rx antenna array element *not in-phase*. Hence, the actual signal amplitude and phase become important.

As Tx splits the original signal of the average power P_{Tx} and maximum amplitude A_{Tx} into N^2 identical signal components with the powers $P_{\text{C}} = P_{\text{Tx}}/N^2$, then the corresponding maximum amplitudes of one signal component, A_{C}, is $A_{\text{C}} = A_{\text{Tx}}/N$. Hence, the combined received signal, $S_{\text{Rx},1}(t)$ is given in (4).

Recalling that the average signal power of a time-variant amplitude $S_{\text{Rx},1}(t)$ is $\text{E}\left[(S_{\text{Rx},1}(t))^2\right]$, we get the average power of the receiver signal in the THz near field, $P_{\text{Rx},1}$, as in (5). *We refer to (4) and (5) as Model 1.*

B. Simplified Theoretical Model

Although Model 1 is exact, (4) and (5) involve *quadruple sums* making the model computationally intensive for large values of N. Further simplifications arise from accounting for the properties of the considered scenario in Fig. 1. *First*, both the phase shift and the attenuation over an individual path depend only on the length of that path, not its location. *Second*, the length of the individual path $d_{(i,j)\to(a,b)}$ depends not on the absolute values of i, j, a, and b, but only on their differences $\Delta X = |i - a|$ and $\Delta Y = |j - b|$, so for constant k and z:

$$d_{(i,j)\to(a,b)} = d_{(i-k,j-z)\to(a-k,b-z)} = d_{(0,0)\to(\Delta X,\Delta Y)}. \tag{6}$$

Hence, as $d_{(0,0)\to(\Delta X,\Delta Y)}$ depends only on ΔX and ΔY, we drop $(0, 0)$ to simplify the notation and just use $d_{(\Delta X,\Delta Y)}$ instead of $d_{(0,0)\to(\Delta X,\Delta Y)}$ further:

$$d_{(\Delta X,\Delta Y)} = \sqrt{d^2 + \frac{c^2}{4f^2}(\Delta X)^2 + \frac{c^2}{4f^2}(\Delta Y)^2}. \tag{7}$$

Finally, as one may observe, the system in Fig. 1 features inherent symmetry: there are many individual paths with

$$S_{\mathrm{Rx},1}(t)=\sum_{i=1}^{N}\sum_{j=1}^{N}\sum_{a=1}^{N}\sum_{b=1}^{N}\left(\frac{1}{N}\sqrt{\frac{2P_{\mathrm{Tx}}}{N^2}\left(\frac{c}{4\pi f d_{(i,j)\to(a,b)}}\right)^2}\cos\left(2\pi f\left[t-\frac{d_{(i,j)\to(a,b)}}{c}\right]\right)\right)=$$
$$=\frac{\sqrt{2P_{\mathrm{Tx}}}}{N^2}\left(\frac{c}{4\pi f}\right)\sum_{i=1}^{N}\sum_{j=1}^{N}\sum_{a=1}^{N}\sum_{b=1}^{N}\left(\frac{\cos\left(2\pi f\left[t-\frac{d_{(i,j)\to(a,b)}}{c}\right]\right)}{d_{(i,j)\to(a,b)}}\right)=$$
$$=\frac{\sqrt{2P_{\mathrm{Tx}}}}{N^2}\left(\frac{c}{4\pi f}\right)\sum_{i=1}^{N}\sum_{j=1}^{N}\sum_{a=1}^{N}\sum_{b=1}^{N}\left(\frac{\cos\left(2\pi f\left[t-\frac{d_{(i,j)\to(a,b)}}{c}\right]\right)}{d_{(i,j)\to(a,b)}}\right). \tag{4}$$

$$P_{\mathrm{Rx},1}=\frac{2P_{\mathrm{Tx}}}{N^4T}\left(\frac{c}{4\pi f}\right)^2\int_{-T/2}^{T/2}\left[\sum_{i=1}^{N}\sum_{j=1}^{N}\sum_{a=1}^{N}\sum_{b=1}^{N}\left(\frac{\cos\left(2\pi f\left[t-\frac{d_{(i,j)\to(a,b)}}{c}\right]\right)}{d_{(i,j)\to(a,b)}}\right)\right]^2\mathrm{d}t. \tag{5}$$

$$S_{\mathrm{Rx},2}(t)=\frac{\sqrt{2P_{\mathrm{Tx}}}}{N^2}\left(\frac{c}{4\pi f}\right)\Bigg[N^2\left(\frac{\cos\left(2\pi f\left[t-\frac{d}{c}\right]\right)}{d}\right)+4\sum_{\Delta X=1}^{N-1}N(N-\Delta X)\left(\frac{\cos\left(2\pi f\left[t-\frac{d_{(\Delta X,0)}}{c}\right]\right)}{d_{(\Delta X,0)}}\right)+$$
$$+4\sum_{\Delta X=1}^{N-1}\sum_{\Delta Y=1}^{N-1}(N-\Delta X)(N-\Delta Y)\times\left(\frac{\cos\left(2\pi f\left[t-\frac{d_{(\Delta X,\Delta Y)}}{c}\right]\right)}{d_{(\Delta X,\Delta Y)}}\right)\Bigg]. \tag{11}$$

different i, j, a, and b, but the same ΔX and the same ΔY. There are $K_0=N^2$ "direct" paths, ($\Delta X=\Delta Y=0$).

Deriving the number of other categories of paths is more complicated but is still possible. We start with computing the number of paths in the horizontal setup $K_{\mathrm{H}}(\Delta X)$, where $\Delta Y=0$, while $\Delta X\neq 0$. For a given row index, the number of available paths of length ΔX is equal to $N-\Delta X$. As there are N equivalent rows in the Tx 2D array, the quantity grows to $N(N-\Delta X)$. Further, for each of the paths with the shifts $(\Delta X,0)$ ($a>i$), there is a "flipped" (symmetric) path directing the other side $a<i$ but leading to the same $\Delta X=|i-a|$. Hence, the total number of horizontal shifts is twice larger than $N(N-\Delta X)$. Finally, for square $N\times N$ arrays, all vertical shifts $(0,\Delta Y)$ are equivalent to their corresponding horizontal shifts $(\Delta X,0)$, where $\Delta X=\Delta Y$. Hence, all the vertical shifts can be replaced with their identical horizontal shifts leading to the total number of paths with shifts $(\Delta X,0)$ or $(0,\Delta X)$ as

$$K_{\mathrm{H}}(\Delta X)=4N(N-\Delta X). \tag{8}$$

Having computed the number of available direct paths K_0 and paths with a horizontal/vertical shift of ΔX, $K_{\mathrm{H}}(\Delta X)$, we proceed with the last category of available paths presented in Fig. 1 – diagonal shifts with $\Delta X\neq 0$ and $\Delta Y\neq 0$. For diagonal shifts, the number of available paths K_{D} depends on both ΔX and ΔY, but can be computed using the same approach as for horizontal shifts: for given $(\Delta X,\Delta Y)$ there are $(N-\Delta X)(N-\Delta Y)$ possible combinations in Fig. 1. For each of those, there are three more rotations possible: $a<i\cup b>j$, $a>i\cup b<j$; and $a<i\cup b<j$. Hence, the total number of diagonal paths with shift $(\Delta X,\Delta Y)$, K_{D} is

$$K_{\mathrm{D}}(\Delta X,\Delta Y)=4(N-\Delta X)(N-\Delta Y). \tag{9}$$

Finally, the computations in Model 1 can thus be simplified using K_0, K_{H}, and K_{D} obtained above. Specifically, instead of adding all N^4 paths individually as in (4) and (5), a simpler approach is through a weighted sum of path categories as:

$$S_{\mathrm{Rx},2}(t)=\frac{\sqrt{2P_{\mathrm{Tx}}}}{N^2}\left(\frac{c}{4\pi f}\right)\Bigg[K_0L_0+\sum_{\Delta X=1}^{N-1}K_{\mathrm{H}}(\Delta X)L_{\mathrm{H}}(\Delta X)+$$
$$+\sum_{\Delta X=1}^{N-1}\sum_{\Delta Y=1}^{N-1}K_{\mathrm{D}}(\Delta X,\Delta Y)L_{\mathrm{D}}(\Delta X,\Delta Y)\Bigg], \tag{10}$$

where L_0, $L_{\mathrm{H}}(\Delta X)$ and $L_{\mathrm{D}}(\Delta X,\Delta Y)$ are the received signal functions related to the length of the corresponding path category (direct, horizontal, and diagonal, respectively).

After substituting $K_0=N^2$, K_{H} from (8), and K_{D} from (9) into (10) and performing simplifications, the following form for $S_{\mathrm{Rx},2}(t)$ (*Simpler Model 2*) is obtained in (11).

The received power following Model 2 is estimated as:

$$P_{\mathrm{Rx},2}=\frac{1}{T}\int_{-T/2}^{T/2}\left[S_{\mathrm{Rx},2}^2(t)\right]\mathrm{d}t. \tag{12}$$

By cross-comparing (4) in Model 1 with (11) in Model 2, one may observe that the approach in Model 2 still includes summation over N. However, the quadruple sums in (4) are now reduced to no more than double summation in (11). Hence, despite a slightly more complex equation in the sum (an extra multiplication) *the asymptotic complexity over N decreases from $\mathcal{O}(N^4)$ in Model 1 down to $\mathcal{O}(N^2)$ in Model 2*.

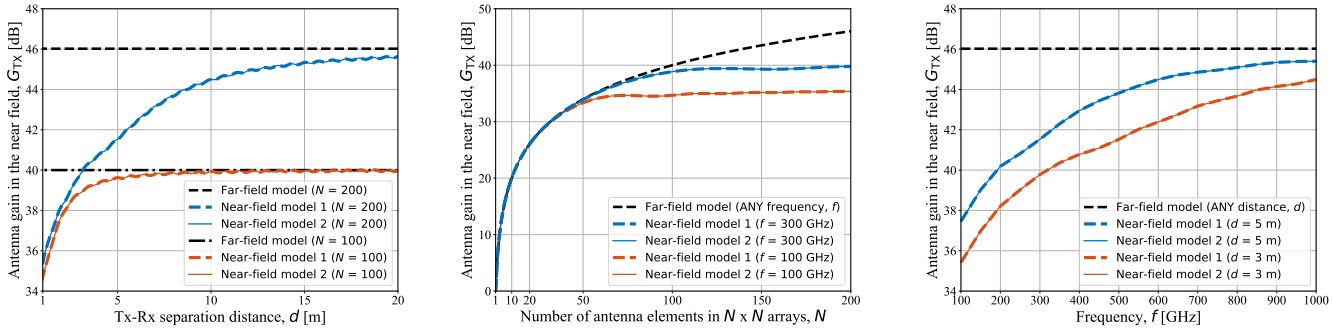

(a) Distance, d; $f = 300\,\text{GHz}$ (b) Number of elements, N; $d = 3\,\text{m}$ (c) Frequency, f; $N = 200$

Fig. 2. Antenna gain, G, as a function of key input parameters in the THz near field.

We finally use the structure in (1) and derive antenna gains in the THz near field for Model 1, G_1, and Model 2, G_2:

$$G_1 = \frac{4\pi f d}{c}\sqrt{\frac{P_{\text{Rx},1}}{P_{\text{Tx}}}}, \quad G_2 = \frac{4\pi f d}{c}\sqrt{\frac{P_{\text{Rx},2}}{P_{\text{Tx}}}}. \tag{13}$$

IV. Numerical Results

Recall, that the total power loss of a THz communication link in the THz near field can be decomposed into: (i) conventional far-field spreading loss and (ii) *distance-dependent* value of the antenna gains in the THz near field. The first component – spreading loss – depends only on the signal frequency, f, and the separation distance between the Tx and Rx antennas, d. However, the second component – *near-field antenna gain* – depends not just on the number of array elements per row and column, N (as it is the case in the far field [3]), but on the combination of three parameters: (i) number of array elements, N, (ii) carrier frequency, f, and (iii) the distance between the Tx and Rx THz arrays, d. Hence, as per (13), the gain of the THz antenna gain in the near field also becomes *frequency-dependent* and *distance-dependent*.

A. The effect of separation distance, d

We start the numerical analysis with Fig. 2(a) illustrating the effective gain of the THz Tx antenna array in the THz near field as a function of the separation distance between the Tx and Rx, d. We particularly compare the canonical far-field gain value from (1) with the near-field results derived in this paper, $G_{\text{Tx},1}$ for Model 1 and $G_{\text{Tx},2}$ for simplified Model 2 using (13). For illustrative purposes, we set the frequency in-between sub-THz and THz bands at $f = 300\,\text{GHz}$ and also compare two sizes of antenna arrays: $N = 100$ and $N = 200$.

As observed from Fig. 2(a), the far-field gain values for $N = 100$ and $N = 200$ expectedly stay constant over distance, d, as they depend only on the number of antenna elements. Contrarily, the effective gain results in the THz near field are notably less trivial. First, for short-range THz communication scenarios (distances under 10 m) the curves stay *up to* 10 *dB lower* than the far-field model predicts. Hence, this figure illustrates the importance of accounting for the near-field propagation effects when analyzing THz communication links over short distances. On the opposite side, with the distance increase (getting closer to the far-field boundary), the results following our near-field models expectedly tend to the level set by the far-field model. Finally, it is worth noting that (as Model 2 presents just a simplified version of the equation giving the exact solution in Model 1) the results of both models match over the entire range of input parameters.

B. The effect of the number of antenna elements, N

We now proceed with Fig. 2(b) showing the one side (Tx or Rx) antenna gain in the THz near-field as a function of the number of antenna array elements. For illustration, we set the Tx-Rx separation distance to $d = 3\,\text{m}$ and compare two frequencies in the sub-THz range: (i) $f = 100\,\text{GHz}$ and (ii) $f = 300\,\text{GHz}$. The far-field gain, G_{FF}, in this figure grows linearly over the total number of array elements, N^2. Notably, G_{FF} is the same for 100 GHz and 300 GHz (as well as any other carrier frequency), as the far-field antenna gain depends only on the number of elements in the array, not the frequency.

Proceeding with the near-field curves for 100 GHz and 300 GHz, we observe that until approximately $N \approx 50$, the values follow the same trend as the far-field model. The reason is that the physical size of the sub-THz antenna of e.g., 10×10 elements is still too small to imply the near-field propagation effects at 3 m (as the near-field zone is still too short). In contrast, beginning from approximately $N \approx 50$, the corresponding near-field values start deviating notably from the ones following the far-field gain curve. The deviation further grows with N reaching around 1 dB for $N = 55$ at 100 GHz and to extremely noticeable 11.5 dB difference (on each side, so 23 *dB difference for both Tx and Rx gains together*) for 100 GHz and 200×200 array.

The results for the higher frequency of 300 GHz follow the same trend, but are slightly less drastic: the visible deviation from the far-field model results starts at larger N values and the maximum difference at $N = 200$ is around 6 dB versus 11.5 dB at 100 GHz. This is because the physical dimensions of the sub-THz antenna array (with $\lambda/2$ element spacing) with the same number of elements are three times smaller at 300 GHz than at 100 GHz leading to nine times shorter near-field zone as per Fraunhofer distance [3] and thus notably less profound near-field effects at a given d. Still, the 6 dB difference in the gain leads to the 12 dB difference in the link budget, which is a huge deviation from the far-field theory.

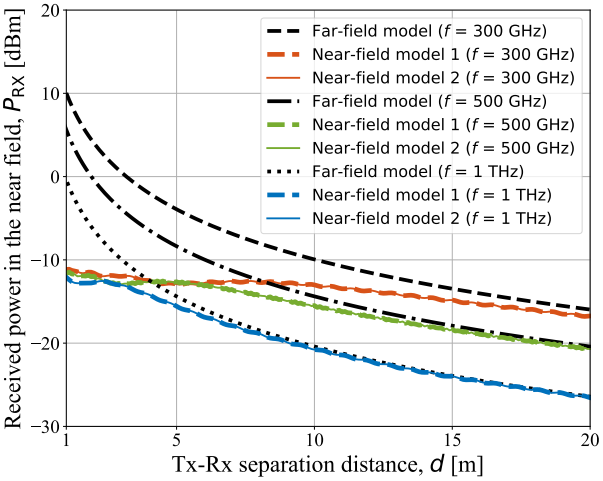

Fig. 3. Received power, P_{Rx}, in the THz near field; $N = 200$.

C. The effect of the signal frequency, f

We finally analyze Fig. 2(c) presenting the antenna gain as a function of the signal frequency, f, for a given size of the antenna array, $N = 200$, and two Tx-Rx separation distances: (i) $d = 3\,\text{m}$ and (ii) $d = 5\,\text{m}$. As observed from Fig. 2(c), the far-field gain does not depend on the separation distance, as per (1), hence the far-field results for 3 m and 5 m are same. This is however not the case for the gains in the THz near-field. As illustrated in the same figure the difference is 2 dB–3 dB between the results at 3 m and 5 m across the selected frequency range. We finally note that the deviation between the canonical far-field path loss and the proposed detailed near-field models in the THz near-field is noticeable across the entire range of sub-THz/THz frequencies in Fig. 2(c). The difference is especially large at shorter distances ($d = 3\,\text{m}$) and lower frequencies, e.g., closer to 100 GHz, as the physical dimensions of the array are larger there implying more severe near-field effects on the received THz signal. Still, even at $f = 1$,THz, where the 200×200 antenna array is only $6\,\text{cm} \times 6\,\text{cm}$, there is still a visible difference of $\approx 2\,\text{dB}$ and $\approx 0.8\,\text{dB}$ on each side for 3 m and 5 distances respectively.

D. Received power in the THz near field, P_{Rx}

We conclude the numerical study with Fig. 3 exploring the dependency between the received power over a THz communication link for $N = 200$ and three signal frequencies: 300 GHz, 500 GHz, and 1 THz, respectively. We observe the non-monotonic behavior of the received power in the THz near field, especially in the range between 1 m and 5 m. This behavior is caused by effects similar to those observed for two-ray propagation models, where the signal components from different Tx antenna array elements come at the Rx either in-phase or out-of-phase depending on the separation distance.

As also observed from Fig. 3, the deviation between the existing far-field model and the proposed near-field models is up to 20 dB and more for shorter distances and gets under 1 dB only after approximately 20 m. This range is expected to constitute a significant part of prospective sub-THz 6G and beyond 6G THz access networks. Hence, in selected future scenarios (e.g., THz WLANs), the near-field-specific propagation effects must be accounted for.

V. Conclusions

Near-field propagation effects present one of the principal novelties when upgrading from state-of-the-art 5G-grade millimeter wave mobile communication systems to prospective 6G/beyond-6G wireless systems operating in the sub-THz and THz bands. In this article, an accurate-by-design approach is presented to mathematically characterize the effective gain of the THz antenna and the corresponding received power for a given separation distance between the transmitter and the receiver in the THz near field. Our study reveals that applying the canonical far-field models when analyzing the THz near-field propagation leads to substantial errors, as the mismatch between the presented two near-field-specific models and the conventional far-field ones may reach several tens of decibels.

The proposed near-field models are much easier to use for telecommunication engineers than existing EM simulation techniques based on Maxwell's equations, as they only operate well-established parameters, such as the separation distance, the frequency, and the antenna array size without the need to parameterize and perform full-fetched EM simulations. The contributed approach can be further extended to account for beam steering or more sophisticated scenario geometries thus forming a solid base for further research on near-field sub-THz and THz communication systems in 6G and beyond.

Acknowledgements

The work has been supported in part by the NSF CNS-2225590 and the Academy of Finland Project EMERGENT.

References

[1] Q. Xue, C. Ji, S. Ma, J. Guo, Y. Xu, Q. Chen, and W. Zhang, "A survey of beam management for mmWave and THz communications towards 6G," *IEEE Communications Surveys & Tutorials*, pp. 1–1, 2024.

[2] M. Cui, Z. Wu, Y. Lu, X. Wei, and L. Dai, "Near-field MIMO communications for 6G: Fundamentals, challenges, potentials, and future directions," *IEEE Communications Magazine*, vol. 61, pp. 40–46, January 2023.

[3] C. A. Balanis, *Antenna theory: Analysis and design*. Wiley, 2016.

[4] S. Basharat, M. Khan, M. Iqbal, U. S. Hashmi, S. A. R. Zaidi, and I. Robertson, "Exploring reconfigurable intelligent surfaces for 6G: State-of-the-art and the road ahead," *IET Communications*, vol. 16, pp. 1458–1474, June 2022.

[5] H. Zhang, N. Shlezinger, F. Guidi, D. Dardari, and Y. C. Eldar, "6G wireless communications: From far-field beam steering to near-field beam focusing," *IEEE Communications Magazine*, vol. 61, pp. 72–77, April 2023.

[6] A. Singh, V. Petrov, H. Guerboukha, I. V. Reddy, E. W. Knightly, D. M. Mittleman, and J. M. Jornet, "Wavefront engineering: Realizing efficient terahertz band communications in 6G and beyond," *IEEE Wireless Communications*, vol. 31, pp. 133–139, June 2024.

[7] V. Petrov, J. M. Jornet, and A. Singh, "Near-field 6G Networks: Why mobile terahertz communications MUST operate in the near field," in *Proc. of the IEEE GLOBECOM*, pp. 3983–3989, December 2023.

[8] C. Girard and A. Dereux, "Near-field optics theories," *Reports on Progress in Physics*, vol. 59, p. 657, May 1996.

[9] P. Monk *et al.*, *Finite element methods for Maxwell's equations*. Oxford University Press, 2003.

[10] P. Boronin, V. Petrov, D. Moltchanov, Y. Koucheryavy, and J. M. Jornet, "Capacity and throughput analysis of nanoscale machine communication through transparency windows in the terahertz band," *Nano Communication Networks*, vol. 5, pp. 72–82, June 2014.